Coupling of the land surface model CAS-LSM with the climate system model CAS-FGOALS-g3

Jinbo Xie[1], Zhenghui Xie[1,2], Binghao Jia[1,2], Peihua Qin[1,2], Bin Liu[1,2], Longhuan Wang[1,2], Yan Wang[1,2], Ruichao Li[1,2], and Si Chen[1,2], Shuang Liu[1,5], Yujing Zeng[1,3], Junqiang Gao[1,4], Lijuan Li[1], Yongqiang Yu[1], Li Dong[1], Zhipeng Xie[6]

[1]State Key Laboratory of Numerical Modeling for Atmospheric Sciences and Geophysical Fluid Dynamics, Institute of Atmospheric Physics, Chinese Academy of Sciences, Beijing 100029, China;

[2]College of Earth and Planetary Sciences, University of Chinese Academy of Sciences, Beijing 100049, China;

[3]Program in Atmospheric and Oceanic Sciences, Princeton University, Princeton, NJ 08544, USA;

[4]School of Mathematics and Statistics, Nanjing University of Information Science and Technology, Nanjing 210044, China;

[5]Key Laboratory of Mountain Hazards and Earth Surface Process, Institute of Mountain Hazards and Environment, Chinese Academy of Sciences, Chengdu 610041, China;

[6]Key Laboratory of Tibetan Environment Changes and Land Surface Processes, Institute of Tibetan Plateau Research, Chinese Academy of Sciences, Beijing 100101, China

Submitted to Journal of Advances in Modeling Earth Systems (JAMES)

Correspondent author: Zhenghui Xie (zxie@lasg.iap.as.cn)

Key Points:

- The land surface model CAS-LSM was implemented into the climate system model CAS-FGOALS-g3.
- The new combined model considered the effects of lateral flow, water use, nitrogen discharge and river transport, freeze thaw fronts, and urban planning.
- Those processes, and human activities, affected the land-energy fluxes and climate by changing the soil moisture.

Abstract:

The land surface model of the Chinese Academy of Sciences (CAS-LSM), which includes lateral flow, water use, nitrogen discharge and river transport, soil freeze thaw front dynamics, and urban planning, was implemented into the Flexible Global Ocean-Atmosphere-Land System model grid-point version 3 (CAS-FGOALS-g3). Simulations were conducted using the land–atmosphere component setup of CAS-FGOALS-g3. The simulations showed reasonable distributions of the land surface variables when compared against observations (including reanalysis, merged data, remote sensing, etc). In terms of the new capabilities, it was shown that considering the groundwater lateral flow caused a deepening of the water table depth of around 25–50 mm in North India, central USA, and Sahel. Including the anthropogenic groundwater use also led to increased latent heat fluxes of about 20 W·m^{-2} in the aforementioned three areas. Inclusion of the soil freeze thaw front (FTF) dynamics enabled seasonal-variation simulations of the freeze and thaw processes, and the FTF-derived permafrost extent was comparable to that seen in the observations. The simulations conducted using the riverine nitrogen transport and human activity schemes showed that major rivers around the globe, including western Europe, eastern China, and the Midwest of the USA experienced annual dissolved inorganic nitrogen (DIN) rates of 25–50 Gg·N·yr^{-1}, which were accompanied by surface water regulation DIN losses of around 28 mg·N·m^{-2}·yr^{-1} and DIN retention of 200–500 mg·N·m^{-2}·yr^{-1}. The results suggest that the model is a useful tool for studying the effects of land-surface processes on the global climate, especially those influenced by human interventions.

Plain Language Summary:

The land surface model of the Chinese Academy of Sciences (CAS-LSM), which includes lateral flow, water use, nitrogen discharge and river transport, soil freeze thaw front dynamics, and urban planning, was implemented into the Flexible Global Ocean-Atmosphere-Land System model grid-point version 3 (CAS-FGOALS-g3). Simulations conducted using the updated model showed reasonable distributions in the land surface variables when compared against observations. The new capabilities of the model with the implementation of the CAS-LSM were also assessed. The results suggest that the model is a potentially useful tool for studying the effects of land-surface processes on the global climate, especially those influenced by human interventions.

1. Introduction

During the past several decades, anthropogenic impacts on climate have received tremendous attention in the climate-research community and in the public domain (Solomon et al. 2007). Human activities that influence the local and global climate can be divided into two main categories: changes in the atmospheric composition, including greenhouse gases and aerosols, and changes at the surface caused by urbanization, agriculture and irrigation, and deforestation (e.g., Pielke and Avissar 1990; Kanamaru and Kanamitsu 2008). Agricultural activities, including water withdrawal and irrigation, can significantly affect the energy and water exchanges between the land surface and the atmosphere by altering the flow regimes of both surface water and groundwater (Shah 2014; Zeng et al. 2016). These effects can enhance the local latent heat flux and thus affect the atmospheric circulation at local and global scales (Yu et al. 2014; Zou et al. 2014; Zeng et al. 2017). The exploitation and withdrawal of groundwater can lead to changes in the lateral flow and transport of groundwater from surrounding areas to local groundwater depressions, thus offsetting the loss of locally stored water (Xie et al. 2012; Fan 2015), and influencing latent heat flux and transpiration partitioning through groundwater redistribution (Maxwell and Condon 2016) that may affect the climate at local and larger scales (Maxwell et al. 2007; Maxwell and Kollet 2008). Anthropogenic nitrogen discharge from fertilizer applications, fossil fuel consumption, and crop production (Galloway et al. 2004), can be transferred and transported in soil and rivers, which may affect the development of biocenoses and ecosystem connections between land and oceans (Jickells 1998). It has also been shown that the discharge and transport of nitrogen can be regulated by human intervention (Maavara et al. 2015; Woli, Hoogenboom and Alva 2016; Van Cappellen and Maavara 2016; Liu et al. 2019).

Denitrification in river and stream sediments is becoming increasingly recognized as an important source of N_2O to the atmosphere (Beaulieu et al. 2011; Ivens et al. 2011). Activities that accompany urbanization, such as anthropogenic heat release (AHR) and urban water usage (UWU), along with the impact of urban spatial structures on the boundary layer, affect the local weather and climate (Sailor et al. 2004; Sailor 2011; Hendel et al. 2015; Hendel et al. 2016; Ketterer et al. 2017). The movement of freeze thaw fronts (FTFs), on the other hand, is an indicator of the climate status, which in turn affects the climate; this freeze and thaw process alters both the carbon-nitrogen cycle and the energy and water exchanges between the land surface and the atmosphere by affecting the soil's hydrothermal characteristics, especially in frozen-soil regions (Zhang 2005; Iwata et al. 2010). These processes are closely impacted by the climate, and in turn affect the climate. Understanding these complex processes, and reasonably representing them in land-surface and global climate models, is very important for providing insights into weather and climate impacts of societally relevant quantities, such as water availability, environmental protection, and other ecosystem services (Wood et al. 2011; Tian et al. 2016; Xie et al. 2016; Bonan and Doney 2018).

Groundwater affects convection, advection, and precipitation by affecting the water-heat flux between the land and atmosphere (Chen and Hu 2004a; Haddeland et al. 2006; Zeng et al. 2016b). A number of studies in recent years have discussed incorporating groundwater lateral flow (GLF) into models (Xie et al. 2012; Fan et al. 2013; Maxwell and Condon 2016; Xie et al. 2018). Zeng et al. (2016) incorporated GLF into a LSM to investigate the effects of stream water conveyance over riparian banks on ecological and hydrological processes. The schemes were also modified to study GLF on global scales (Zeng et al. 2018). As GLF dynamics is often linked with human water use (Zeng et al. 2016; Xie et al. 2017) incorporated schemes describing GLF and human water use to investigate their effect on simulated land-surface processes. Zeng et al. (2017) also incorporated a human water-use (HWR) scheme to investigate the impact of groundwater exploitation on the global climate. Liu et al. (2020), on the other hand, incorporated schemes of anthropogenic heat release, and urban water use, as well as an urban-height scheme that considered height variations in the urban land model to study the effects of these processes on the urban climate. For nitrogen-related processes, Liu et al. (2019) included schemes of riverine dissolved inorganic nitrogen (DIN) transport and human activities, including nitrogen discharging and human water use, into a LSM coupled with a river transport model (RTM). In terms of the soil freeze and thaw processes, the Stefan method was recently incorporated in multilayered systems to simulate FTFs that were subsequently incorporated into a LSM for global simulations by Gao et al. (2016, 2018, 2019). Despite the abovementioned efforts; however, current LSMs do not synchronously describe all of the aforementioned processes, which makes it difficult to fully quantify the degree to which human activities affect the eco-hydrological system and global climate.

To better understand the responses of the Earth system to external forcing changes, and promote climate system model development, the Coupling Model Working Group of the World Climate Research Programme proposed the Coupled Model Intercomparison Project (CMIP). Among the participating models in the most recent phase of this project, CMIP6, CAS-FGOALS-g3 was developed by the State Key Laboratory of Numerical Modeling for Atmospheric Sciences and Geophysical Fluid Dynamics, Institute of Atmospheric Physics, Chinese Academy of Sciences (LASG/IAP), which is considered to be a crucial modeling tool for climate science research (Li et al., 2020). CAS-FGOALS-g3 participates in CMIP6 by providing historical, Diagnostic, Evaluation and Characterization of Klima (DECK) simulations and other CMIP-Endorsed Model Intercomparison Projects (such as Scenarios, Paleo, Land, etc.), and it can serve as a platform as for the evaluation of climate response to anthropogenic forcing.

In this study, we implemented CAS-LSM, which described the aforementioned processes, into the climate system model CAS-FGOALS-g3 to study the impact of these processes on the global hydroclimate. This implementation of CAS-LSM expanded the range of studies with CAS-FGOALS-g3, which allowed us to further assess the impact of the interaction between anthropogenic activities and the eco-hydrologic system, and hence weather and climate.

The remainder of this paper is organized as follows. Section 2 describes the model development, and Section 3 provides the data and experiment design. Section 4 describes the validation of land surface climate simulations using the new CAS-FGOALS-g3 with a focus on variables such as surface air temperature, precipitation, soil water storage, evapotranspiration, river discharge, and the surface albedo, as well as an assessment of snow-albedo feedback. Section 5 describes the new features of CAS-FGOALS-g3 with the implementation of CAS-LSM, and Section 6 gives a discussion and summary.

2. Model Development

2.1 CAS-LSM

Detailed descriptions of the model improvements and the performance of CAS-LSM in the offline mode (i.e., forced with observed meteorology) was mainly documented by Xie et al. (2018). The following series of papers provided reference for the many schemes used here: Xie et al. 2012; Zeng et al. 2016a, 2016b, 2018; Zou et al. 2014, 2015; Zeng et al. 2016b, 2017; Gao et al. 2016, 2019; and Liu et al. 2019. For reference, we have included a schematic diagram that depicts the additional processes and functionality that exists within CAS-LSM (Fig. 1). The schemes for GLF, human water use, FTFs, anthropogenic nitrogen discharge, and urban planning, were implemented into CLM4.5 (Oleson 2013) to produce CAS-LSM, which now considered the abovementioned processes. CLM4.5 was developed by the National Center for Atmospheric Research. This model included bio-geophysical and bio-geochemical mechanisms and energy, and mass fluxes from the land to the atmosphere, and was the land-surface component of the Community Earth System Model 1.2.0 (Hurrell et al. 2013). The bio-geophysical processes included solar and longwave radiation interactions with vegetation canopies and soil, momentum and turbulent fluxes from the canopies and soil, heat transfer in soil and snow, hydrology of canopies, soil, and snow, and stomatal physiology and photosynthesis. The bio-geochemical processes included vegetation photosynthesis, phenology, the carbon and nitrogen cycles, decomposition, and wildfires (Lindsay et al. 2014). Also contained in CLM4.5 was an interactive crop-management model, which simulated crop growth and its effect on land processes. A sub-gridded hierarchy of land units, soil profiles, and plant-function types was used in CLM4.5 to describe the heterogeneity within each grid cell. Different land uses, such as varieties of vegetation, lakes, urban areas, and glaciers, were addressed separately even if they coexist in a given grid cell. The CAS-LSM, building upon CLM4.5, coupled the GLF, HWR, FTFs, AHR, UWU and DIN as optional configurations, with the target being more complete land surface modeling.

2.1.1 Human water use (HWR)

The scheme of HWR was incorporated into CAS-LSM as a sub-model (Zou et al. 2015; Zeng, Xie and Liu 2017). The HWR mainly considered withdrawal due to groundwater pumping, in which the estimated groundwater pumping rate from aquifers was apportioned among agricultural, industrial and domestic use. The industrial and domestic consumptions had two components, where the wastewater produced by industry and human daily life was treated as a discharge into local rivers and the net water consumption was treated as evaporation to the atmosphere. The aquifer recharge rate was updated by subtracting the GW extraction rate from the original aquifer recharge rate; for irrigation consumption, the net water input rate was timed as the ratio of the agricultural consumption rate and added to the top of the soil's surface. The pumping rate and the other ratios were determined by forcing data combined from three data sources, including the Food and Agriculture Organization of the United Nations (FAO) global water information system (http://www.fao.org/nr/water/aquastat/main/index.stm), the Global Map of Irrigation Areas, version 5.0 (Siebert et al. 2005, 2013), and the historical monthly soil moisture and saturated soil moisture simulated by CLM4.5 offline using the atmospheric forcing data set described by Qian et al. (2006) for the years 1965–2000.

2.1.2 Groundwater lateral flow (GLF)

A two-dimensional groundwater (GW) movement equation based on Darcy's Law and the Dupuit approximation (Bear 1972) was used to realize GW exchange between grid cells. The numerical formulation of this equation considered the equal chance of a cell exchanging water with its horizontal neighboring cells from eight directions. The GLF module was calculated in a 1-km-sized cell based on the water table gradients between itself and its neighboring cells, which then updated the groundwater table depths based on both the GLF fluxes and the vertical water flux obtained from CAS-LSM, and the calculated lateral flux was sent back to CAS-LSM to adjust the water table at the coarse land model resolution. A simple resolution conversion method based on the LSM sub-grid structure was used to link CLM4.5 and the GLF module at different resolutions. For the depth-to-bedrock that describes the distance between the ground surface and the less permeable bedrock layers, we used the global data set of depths-to-bedrock at 1-km resolution presented by Shangguan et al. (2017).

2.1.3 Freeze and thaw fronts (FTFs)

For the FTFs, Stefan's equation (Jumikis 1977; Lunardini 1981; Woo et al. 2004; Zhang and Wu 2012; Xie et al. 2013; Gao et al. 2016; Gao et al. 2018) provided a basis to compute one-directional freeze and thaw in a soil column (Jumikis 1978), which was based on heat conduction and assumes that all heat that reached the freezing or thawing front was used for water freezing or melting. This method was frequently used by permafrost scientists to predict frost depth, and to simulate heat transfer during water phase transitions in frozen soil when little site-specific information are available. It could also be applied to calculate one-directional FTFs in a soil profile (Xie and Gough 2013; Gao et al. 2016). The FTFs were implemented into CAS-LSM here following Gao et al. (2018).

2.1.4 Nitrogen transport and human water use

For nitrogen processes, the schemes of human activities (including nitrogen discharge and water regulation) and the riverine DIN transport were incorporated into CAS-LSM via the coupling of the RTM. For nitrogen discharge, the nitrogen fertilizer data were updated using the scheme of Lu and Tian (2017), and the point source pollution was updated using the data merged by Morée et al. (2013). For water regulation, the surface water included the scheme of Hanasaki, Kanae and Oki (2006), and the groundwater scheme follows that of Zou et al. (2015) and Zeng et al. (2016). For the surface water and groundwater, the data were determined from several source data sets, including the Food and Agricultural Organization (FAO) water-use data set (http://www.fao.org/nr/water/aquastat/data/query/index.html), the Global Map of Irrigation Areas, version 5.0 (Siebert et al. 2013), the historical monthly soil moisture levels and saturated soil moisture levels simulated by CLM4.5 offline for the years 1965–2000 (Zeng et al. 2017), and the FAO water information system for 2010 (http://www.fao.org/nr/water/aquastat/main/index.stm). During DIN transport, a proportion of the DIN will be affected by the surface and groundwater regulation based on the mean DIN concentration, and the rate of withdrawal for surface and groundwater (Liu et al. 2019). For the nitrogen river transport, based on the water transport framework in CAS-LSM, the DIN inputs, including soil DIN runoff and leaching, nitrogen deposition, and point source nitrogen discharge, were used as tracers in the nitrogen transport module, along with a DIN retention module during the transport (Nevison et al. 2016). As nitrogen transport is associated with water temperature, this variable was also considered in CAS-LSM following the scheme of van Vliet et al. (2012). Anthropogenic heat discharge from thermoelectric power plants was also considered in CAS-LSM (Liu et al. 2019), where the input data for the emitted heat are from Raptis and Pfister (2016).

2.1.5 Urban planning

Urban planning is concerned with the design and development of urban environments, including population control, transport management, and building distributions. The energy consumption, water usage, and the building construction in a city are closely related to urban planning, which have important effects on the weather and climate by affecting the energy, water cycle, and urban meteorology. In CAS-LSM, the schemes of AHR, UWU, and urban roughness height (and height variations) were incorporated to consider the effects of these processes.

AHR was treated as part of the sensible heat flux that affected the energy balance equation. AHR could be divided into four components: AHR from vehicles, the building sector, industry, and human metabolism (Sailor and Lu 2004), representing the major sources of waste heat in the urban environment. As anthropogenic heat is closely tied to energy consumption (Sailor 2011), the AHR from vehicles, buildings, and industry could be estimated by listing all kinds of energy consumption (including coal, coke, crude oil, gasoline, kerosene, diesel, fuel oil, natural gas, and electric power). For UBU, a simple UBU scheme, including urban irrigation and road sprinkling, was incorporated into the CAS-LSM model based on the scheme described by Zeng et al. (2017). Here, ecological and farmland irrigations were both treated as urban irrigation, and the road sprinkling scheme was activated at night during the summer when water was applied to the impervious road layer to accelerate evaporation. For the urban roughness height, this parameter is affected by building construction, and the spatial distribution of urban building heights, which can affect the heat and momentum variables. Here, the scheme was based on the work of Millward-Hopkins et al. (2011). It is worth noting that because urban planning is currently used only in the regional setup, it was set as an option in the model and not used in the global coupled simulations.

2.2 Coupling CAS-LSM with CAS-FGOALS-g3

CAS-FGOALS-g3 is a global climate model consisting of atmosphere (Li et al. 2019), land (Xie et al. 2018), oceans (LICOM) and a sea-ice model (Holland et al. 2012). A general overview of CAS-FGOALS-g3 has been provided by Li et al. (in preparation). The land component of CAS-FGOALS-g3 was CAS-LSM (Xie et al. 2018), which included the aforementioned processes including GLF (Xie et al. 2012; Zeng et al. 2016a, 2016b, 2018), human water exploitation (Zou et al. 2014, 2015; Zeng et al. 2016b, 2017), FTFs (Gao et al. 2016, 2019), river nitrogen transport and human water use (Liu et al. 2019), and urban planning. Additional input land-use data sets have also been included in CAS-LSM, and the human water use, urban water use and AHR, and anthropogenic nitrogen discharge are treated as forcing input data in the model.

The coupling of CAS-LSM into CAS-FGOALS-g3 (Fig. 1) was based on CPL7 developed at the National Center for Atmospheric Research (NCAR). Compared with CPL6 (Craig et al. 2005), CPL7 possessed improved memory and performance scaling that could support much higher resolution configurations. In addition, CPL7 had more sophisticated computing resource control and a single executable, which allowed the models to run flexibly and simplified the machine requirements for the dispatcher. The land component communicated both state information and fluxes with the atmosphere component through the coupler during every atmospheric time step.

3. Data and Experimental Design

3.1 Experimental design

The main simulations presented here were the five members from the Atmospheric Model Inter-comparison Project (AMIP) protocol simulation (for the period 1979–2014), three groups of simulations named CTL, LC, and LGC (corresponding to the use of the FTF, FTF and HWR, FTF, HWR and GLF modules), and an additional single member simulation of the land-atmosphere coupled simulation named NP (Table 1). The AMIP simulations were performed using the time-varying external forcing recommended by CMIP6 (https://esgf-node.llnl.gov/search/input4mips/). The atmosphere and land resolution was 2° in both latitude and longitude in these simulations, and the monthly observations of the sea surface temperatures (SSTs) and sea ice concentration from the HadISST data set (Rayner et al. 2003) were used for prescribing the ocean surface conditions. The forcing for the AMIP runs included the monthly mean total solar irradiance (TSI) (Matthes 2017), greenhouse gas (GHG) concentrations, including latitudinal changes and seasonality (Meinshausen et al. 2017), ozone concentrations, anthropogenic aerosol optical properties and the associated Twomey effect (Stevens 2017), land use changes (Land Use Harmonization v2, http://luh.umd.edu/), and historical stratospheric aerosols. In addition, the anthropogenic groundwater exploitation forcing data from 1965–2014 were added (Zeng et al. 2017).

For the AMIP runs, there were five members that shared the same setup, but which had different initial conditions. The simulation time for the AMIP runs was 1979–2014. For the CTL, LC and LGC simulations, they generally followed a similar setup to the AMIP runs, except that the simulation time for these runs was for a 41-year duration from 1976 to 2010 (using the period 1970–75 for spin-up). To reduce the internal noise, and enhance the forced signal caused by the HWR and GLF, ensemble averages were used here, where each group of experiments contained three ensemble simulations using different initial conditions, the results of which were then averaged over the ensemble for evaluation (Koster et al. 2002, 2006). In the current study, three individual simulations, typically differing only in their initial atmospheric and land surface conditions, comprised each ensemble (CTL, GC, or LGC). Simulations with corresponding ensemble members in the three sets of simulations typically shared the same initial conditions (for instance, CTL1, LC1, and LGC1 shared the same initial conditions). For the NP transport simulation, it generally followed a similar setup to the AMIP runs, except that the bio-geochemical module and nitrogen transport module were opened to obtain the nitrogen transport-related variables. The simulation time for this simulation was 1960–2014.

3.2 Observational data

The 2-m temperature data consisted of the 0.5° × 0.5° land temperature data compiled by Cort Willmott and Kenji Matsuura of the University of Delaware from a large number of stations from Global Historical Climate Network and the archive of Legates and Willmott (Willmott and Matsuura 2001). The precipitation observations were obtained from CMAP, which are from the Climate Prediction Center (CPC) Merged Analysis of Precipitation 1979–2009 monthly time series, which have a resolution of 2.5° × 2.5° (Xie and Arkin 1997). The latent heat observational data were from FLUXNET-MTE (Jung et al. 2009, 2010). The FLUXNET-MTE data were from the FLUXNET network of eddy covariance towers, which were upscaled to monthly data on a 0.5° × 0.5° grid (Jung et al. 2010) using the model tree ensemble (MTE) approach described by Jung et al. (2009) (1982–2004 average). For the soil moistures, the Global Land Data Assimilation System version 2 (GLDAS 2) data were used (Rodell et al. 2004). The Moderate Resolution Imaging Spectroradiometer (MODIS) all-sky albedos were derived from the black-sky (direct) and white-sky (diffuse) near-infrared and visible wave band albedos by weighting them according to the CAS-LSM partitioning of solar radiation into these components.

The MODIS data were from collection 4, which were the climatological average of the years 2001–2003.

4. Simulations and Assessment

4.1 Surface air temperature and precipitation

The ensemble mean climatological annual cycle of the surface air temperature (T_{air}) and precipitation (P) for nine representative high-latitude, midlatitude, and tropical regions for CAS-FGOALS-g3, and the observational estimates for both variables, are shown in Fig. 2 and Fig. 3, respectively. For the G3 simulations of the temperature, the overall results showed that the annual cycle of the G3 simulations in the nine regions mimicked the observations. Among the comparisons, the simulated temperature seasonal cycle data were at high-latitude and mid-latitude regions were closer to the observations than those of the tropical regions, where the Amazon region depicted a high temperature bias in JFM (January to March) and SON (September to November), the Sahel region depicted a lower temperature bias in MAM (March to May) and SON, and the Indian region depicted a systematically higher seasonal cycle (Fig. 2).

Inspection of the regionally averaged seasonal cycles of precipitation are shown in Fig. 3. Unlike that of the temperature, comparison of the regionally averaged seasonal cycles of precipitation with the observations do not show obvious trends at specific latitudes. Systematic overestimations of precipitation appeared in Alaska and the Amazon, and the seasonal cycle was too low and did not follow the phase of the observations in central Canada. For places like the eastern USA and Europe, the seasonal cycle was out of phase with the observations. For Sahel, on the other hand, an earlier peak of the cycle appeared in May, rather than in August in the observations. Overall, the seasonal cycle of precipitation depicted poorer results than that of the temperature seasonal cycle, and this bias of the seasonal cycle did not show obvious features in terms of latitude.

4.2 Evapotranspiration, soil water storage, and runoff

The seasonal cycle of the regional average latent heat flux is shown in Fig. 4. Generally, the CAS-LSM simulated values of the latent heat flux followed the observations, except with an overall underestimation in the nine representative regions. The general underestimation of the seasonal cycle was apparent, except for Amazon, which generally followed that of the observations (although with an underestimated climatology). Overall, the peaks of the seasonal cycle were smaller in the other eight places relative to those seen in the observations, among which India displayed the worst result.

The differences in the mean soil water content between MAM and SON between the model simulation and GLDAS2 (Rodell et al. 2009) are shown in Fig. 5. While the simulations agreed well with the observations in general (Figs. 5(a–b)), the value magnitudes of the simulations were smaller than that of GLDAS2 in regions of the Amazon, southern and central Africa, North America, southern and eastern Asia, and Australia. This indicated weaker seasonal variations in the simulated soil water content. The hydrology and snow parameterization schemes in the LSM may be largely responsible for these biases.

River discharge to oceans in the CAS-LSM simulations was calculated via the RTM (Branstetter and Famiglietti 1999), which transported grid-cell runoff to oceans via pathways that approximate the paths of the real global river network. Overall, the total simulated river discharge into oceans was scattered around the observations (Fig. 6), with some underestimations at some stations, especially in those that have lower annual discharge. As the total discharge into the world's oceans was directly related to land precipitation minus evapotranspiration, these underestimations may be due to precipitation bias in the model. In the simulations, the most poorly simulated large rivers were the Congo and Orinoco Rivers, where far too much discharge was simulated for the Congo River (more than 100% discharge than observed) and far too little discharge from the Orinoco River (less than 50% discharge than observed).

4.3 (Snow) Surface albedo and snow cover extent

The global all-sky snow-free surface albedo has been compared to the MODIS albedo estimates in Fig. 7. The MODIS all-sky albedos were derived from the black-sky (direct) and white-sky (diffuse) near-infrared and visible wave band albedos by weighting them according to the partitioning of solar radiation into these components. The MODIS data were from collection 4, and were the climatological average of years 2001–2003. Overall, the simulated values were quite similar to the MODIS values, except for certain mountain regions like the Tibetan Plateau, the Rocky Mountains and some northern high latitude regions like Siberia and Alaska.

The Northern Hemisphere snow cover extent was also compared with the Northern Hemisphere EASE-Grid Snow Cover and Sea Ice Extent (Brodzik and Armstrong 2013) data, as displayed in Fig. 8. It was seen that CAS-LSM simulated quite well the NH snow cover extent, with an overestimate of the snow near the Tibetan Plateau and minor underestimate in parts of Europe and near-polar regions in North America.

5. New Features in CAS-FGOALS-g3

5.1 Impact of GLF on the water table

Changes in groundwater heads due to activities such as the over-exploitation of groundwater can lead to a decline of the groundwater table and depression cones near wells (Chen et al. 2003, 2011). These can cause changes in the lateral flow, which naturally transports groundwater from surrounding areas to local groundwater depressions. This process plays a critical role in offsetting the loss of locally stored water, and in relieving the negative effects of overexploitation on the eco-hydrological system. The addition of the GLF process allowed for the consideration of the lateral flow, which has been shown to be an important process, especially for the simulation of hydrological variables. Figure 9 shows the simulated equilibrium water table depth with and without GLF (EXP and CTR, respectively), and their difference, for the years 1979–1999. Apparent modification of the groundwater by the GLF module was seen in these figures; the water tables in North Africa, Arabian Peninsula, parts of central Asia, and southern Australia have deepened. Among these, the largest can be seen in North Africa, where the largest depth reached 50 m below ground; small parts of northern India also showed similar deepening phenomena. In other regions, such as the western coast of North America and Australia, the deepening rate was smaller, with values of 35 m and 12 m, respectively. This increased spatial variability of the modeled groundwater table depth in the EXP run may result in differences in the bio-geophysical and bio-geochemical aspects of the land surface (e.g., land atmospheric coupling, water extraction of the vegetation, etc.), and thus had potential effects on the climate process under climate warming.

5.2 Impact of anthropogenic groundwater exploitation on regional climates

The global water demand is rapidly increasing as a result of economic development and population growth (Rodell and Famiglietti 2002; Rodell et al. 2009; Alvarez et al. 2012; Shi et al. 2013; Devic et al. 2014). Groundwater is widely used to supplement human demands for freshwater due to its convenience of extraction and good quality. The continuous over extraction of groundwater resources for consumption not only reduces groundwater table levels, but also changes the regional, and even global, environment and climate (Pokhrel et al. 2012b; Chen and Hu 2004). Implementation of anthropogenic groundwater exploitation in the CAS-FGOALS model was done by using a groundwater exploitation extraction forcing data set, the details of which can be found in the work of Wang et al. (2020). Figure 10 shows the simulated latent heat flux with and without anthropogenic groundwater exploitation (EXP and CTR, respectively). As seen in the figure, addition of the anthropogenic groundwater exploitation has caused the significant latent heat flux to increase (5–20 W·m^{-2}) in three representative over extraction regions of North India, North China, and the western coast and central regions of the USA. According to Dirmeyer et al. (2013), evapotranspiration in these three places was restricted by water availability more than in other regions. Thus, when a greater supply of water was available, more evaporation latent heat occurred. This argued for the explicit representation of anthropogenic groundwater exploitation within climate models.

5.3 Freeze thaw fronts

Freeze-thaw processes in soils, including changes in FTFs, are very sensitive to warming. However, the latest climate models do not predict changes in FTFs directly. Implementation of the FTF module into CAS-FGOALS was performed by generally following the prescription of Gao et al. (2019). We used the maximum thaw depth in permafrost regions as the active layer depth, where its spatial distribution is shown in Fig. 11(a). Although a direct comparison with observations was difficult because no subgrid-scale permafrost representation was currently used in the model, the spatial distribution of the model simulation was still comparable with the maps of permafrost provided by the International Permafrost Association (IPA; Brown et al. 1998) (Figs. 11(a–b)).

In terms of the FTFs, Fig. 12 shows their spatial distribution for February and August, and the seasonal cycle for two points, one in seasonally frozen ground, and another in a permafrost region. The thaw depth was usually the shallowest in February and deepest in August. The simulated thaw depths in February were thus all near the surface, except for a few places near the borders of seasonally frozen ground and permafrost (Fig. 12(a)). In August, the simulated thaw depths presented a decreasing trend as the latitude increased (Fig. 12(b)). The simulated frost depths, on the other hand, showed an opposite trend as seen for the thaw depths. It was seen that the frost depth extended to the south in

February and retreated north in August (Figs. 12(c–d), respectively). Figures 12(e) and 12(f) show the weight-averaged FTF seasonal cycle of two regions (seasonally frozen ground and permafrost, respectively). For the seasonally frozen ground (Fig. 12(e)), the frost depth was deeper in winter and gradually became shallower as time advanced to summer. The thaw depth, on the other hand, starts to melt down in Spring, and gets deeper in May until both the frost and thaw depths meet, then the thaw depth gets shallower again in summer to fall. For the permafrost region (Fig. 12(f)), as the frost depth below is basically frozen all the time, there is only thaw depth that starts to melt in spring and gets deeper through summer, and gets shallower until winter when the thaw depth basically stay on the surface. Overall, the FTFs tended to simulate the seasonal variation of the freeze and thaw process, and the FTF-derived permafrost extent was comparable to that seen in the observations. Thus, the inclusion of FTF was apt for simulations of the seasonal freeze thaw process in seasonally frozen ground and permafrost regions.

5.4 Anthropogenic nitrogen discharge on DIN transport in global rivers

Excess nutrients from fertilizer applications, pollution discharge, and regulated outflow through rivers from lands to oceans, can seriously impact coastal ecosystems. A reasonable representation of these processes in LSMs and RTMs is very important for understanding human–environment interactions. The implementation of the nitrogen transport module in CAS-FGOALS (Fig. 1) was like the coupling process shown in Fig. 1 in Liu et al. (2019). Note that currently the N transport to the ocean is not added and merits future work. Figure 13 shows the forcing of point-source N and its transport in global rivers simulated by CAS-FGOALS-g3. It was seen that several large point sources of N existed around the globe, with three centers including the middle of the USA (Mississippi River), western Europe, and the north of China (Yellow River and Yangtze River). The annual forcing rate of the source N ranges between 1000–8000 $mg \cdot N \cdot m^{-2} \cdot yr^{-1}$.

Corresponding to this forcing, we saw that almost all the large rivers in the world have been affected by widespread human activities (Fig. 7(b)). The rivers in western Europe and eastern China were the most polluted, where the annual DIN increased by 25–50 $Gg\cdot N\cdot yr^{-1}$. The nitrogen discharge by both runoff N and point source could directly and markedly augment the amount of DIN in most rivers across the world, and was hence an important factor related to riverine environmental problems. Undoubtedly, the Mississippi River Basin, Yellow River Basin, Yangtze River Basin, and western Europe were the most effected regions.

The process of N transport within a river is another important process in terms of N transport. The river temperature, which affected the reactions of the N transported in the river, is shown in Fig. 14(a). The river temperatures overall followed a change with latitude, where the temperature decreased as the geographical position extended northward. Another significant feature was the change with altitude, such as the river temperatures in mountain regions like the Tibetan Plateau or the Andes Mountains being lower than those in the surrounding regions. As a result of the river temperature and transport reactions therein, DIN retention in rivers was also shown in Fig. 14(b), where most of the retention was in western Europe, North China, middle USA, and the south-eastern parts of Australia and South America. In addition to N retention, N transport was also impacted by surface water regulation (Fig. 14(c)), which tended to withdraw DIN at large dams. The withdrawn DIN, corresponding to large water-regulation activities such as in northern India, North China, and parts of the USA, are shown in Fig. 14(d). In general, our results suggested that incorporating schemes related to riverine nitrogen transport and human activities into the model could be an effective way to monitor the global river water quality and evaluate the performance of the global land surface modeling. In future work, the developed model in this work will be coupled with atmospheric and ocean models to simulate and project the global nitrogen cycle.

6. Summary and Discussion

In this paper, CAS-LSM, which included lateral flow, water use, nitrogen discharge and river transport, soil freeze thaw front dynamics, and urban planning, was implemented into CAS-FGOALS-g3. When compared against observations, the surface climate CAS-FGOALS-g3 simulations showed reasonable distributions in the land surface variables, including the 2-m temperature, precipitation, latent heat flux, river ocean discharge, soil moisture, snow fraction, and surface albedo. For the temperature, the seasonal temperature cycles at high-latitude and middle latitude regions were closer to the observations than those in tropical regions, while comparison of the regionally averaged seasonal cycles of the precipitation with the observation did not show obvious trends in terms of the latitude. For the other variables, they generally presented an overall reasonable comparison with the observations.

Also assessed were the new capabilities of the model with the implementation the CAS-LSM. Several of these aspects will be evaluated in greater detail that in other papers within the special issue of the Chinese Academy of Sciences Climate and Earth System Models (CAS-FGOALS and CAS-ESM) and Applications special issue in the Journal of Geophysical Research: Atmosphere and the Journal of Advances in Modeling Earth Systems. Apparent modification of the groundwater was introduced by including a GLF module. This allowed us to model the spatial variability of the groundwater lateral flow, which may lead to considerable differences in the bio-geophysical and bio-geochemical aspects of the land surface, and thus have potential effects on climate processes under climate warming. For anthropogenic groundwater use, over extraction in three representative over extraction regions, northern India, North China, and the western coast and central regions of the USA may lead to increased evapotranspiration.

The inclusion of the FTF scheme enabled the model to simulate the seasonal variation of the freeze and thaw process. It was seen that the simulated FTF-derived permafrost extent was comparable to that seen in the observations. Aside from the FTFs, incorporating schemes related to riverine nitrogen transport and human activities into the model was shown to be an effective way to monitor the global river water quality, and evaluate the performance of the global land surface modeling. The overall results of the new scheme suggested that the model was a potentially useful tool for studying the effects of land-surface processes on the global climate, especially those that experience human interventions. In future work, such as the special issue just mentioned, we will present more detailed results of our investigations of the interactions between the land and the atmosphere at large scales.

Acknowledgements

We thank Yang Jiao for transforming the permafrost map data for use. This work was jointly funded by the National Natural Science Foundation of China (Grant No. 41575096), the Key Research Program of Frontier Sciences, Chinese Academy of Sciences (Grant No. QYZDY-SSW-DQC 012), and Grant No. 41806034 from the National Science Foundation of China.

References

Beaulieu, J. J., et al. (2011), Nitrous oxide emissions from denitrification in stream and river networks. *Proc. Natl. Acad. Sci.*, U. S. A., 108, 214–219.

Brodzik, M. J. and R. Armstrong. 2013. Northern Hemisphere EASE-Grid 2.0 Weekly Snow Cover and Sea Ice Extent, Version 4. (Indicate subset used). Boulder, Colorado USA. NASA National Snow and Ice Data Center Distributed Active Archive Center. doi: https://doi.org/10.5067/P7O0HGJLYUQU. (Date Accessed).

Carpenter SR, Stanley EH, Vander Zanden MJ., et al. (2011), State of the World's freshwater ecosystems: physical, chemical, and biological changes. Annu Rev Environ Resour, 36:75–99.

Dai, A., and K. E. Trenberth, (2002), Estimates of freshwater discharge from continents: Latitudinal and seasonal variations. J. Hydrometeorol., 3, 660-687.

Dirmeyer, P. A., Y. Jin, B. Singh, and X. Yan, 2013: Trends in land–atmosphere interactions from CMIP5 simulations. J. Hydrometeor., 14, 829–849, doi:10.1175/JHM-D-12-0107.1.

Gao, J., Xie, Z., Wang, A., et al. (2016). Numerical simulation based on two-directional freeze and thaw algorithm for thermal diffusion model. Applied Mathematics and Mechanics, 37(11), 1467–1478. https://doi.org/10.1007/s10483-016-2106-8

Gao, J., Xie, Z., Wang, A., et al. (2019). A new frozen soil parameterization including frost and thaw fronts in the Community Land Model. Journal of Advances in Modeling Earth Systems, 11, 659–679. https://doi.org/10.1029/2018MS001399

Gleeson T, Wada Y, Bierkens MFP, et al. (2012), Water balance of global aquifers revealed by groundwater footprint. Nature, 488:197–200.

Hendel M, Gutierrez P, Colombert M, et al. Measuring the effects of urban heat island mitigation techniques in the field: Application to the case of pavement-watering in paris(J). Urban Climate, 2016, 16: 43-58.

Hendel M, Royon L. The effect of pavement-watering on subsurface pavement temperatures(J). Urban Climate, 2015, 14: 650-654.

Ivens, W., D. Tysmans, C. Kroeze, A. Loehr, and J. van Wijnen (2011), Modeling global N2O emissions from aquatic systems, Curr. Opin. Environ. Sustain., 3, 350–358.

Jumikis, A. R. (1978). Thermal geotechnics. Soil Science, 125(6), 393. https://doi.org/10.1097/00010694-197806000-00010.

Jung, M., M. Reichstein, and A. Bondeau, (2009), Towards global empirical upscaling of FLUXNET eddy covariance observations: Validation of a model tree ensemble approach using a biosphere model. Biogeosciences, 6, 2001–2013, doi:10.5194/bg-6-2001-2009.

Jung, M., and Coauthors, (2010), Recent decline in the global land evapotranspiration trend due to limited moisture supply. Nature, 467, 951–954, doi:10.1038/nature09396.

Ketterer, C., Gangwisch, M., Fröhlich, D. et al. (2017). Comparison of selected approaches for urban roughness determination based on Voronoi cells. Int J Biometeorol 61, 189–198. https://doi.org/10.1007/s00484-016-1203-2.

Li L. J., Y. Q. Yu, Y. L. Tang, et al., (2020), The Flexible Global Ocean–Atmosphere–Land System Model Grid-Point Version 3 (FGOALS-g3): Description and Evaluation, Journal of Advances in Modeling Earth Systems. https://doi.org/10.1029/2019MS002012.

Liu Shuang, Zhenghui Xie, Yujin Zeng, et al. (2019), Effects of anthropogenic nitrogen discharge on dissolved inorganic nitrogen transport in global rivers. Global change Biology, 2019,00: 1–21.

Maavara, T., Parsons, C. T., Ridenour, C., Stojanovic, S., Dürr, H. H., Powley, H. R., & Van Cappellen, P. (2015). Global phosphorus retention by river damming. Proceedings of the National Academy of Sciences, 112, 15603–15608. https://doi.org/10.1073/pnas.1511797112.

Matthes, K., Funke, B., Andersson, M. E., Barnard, L., Beer, J., Charbonneau, P., et al. (2017). Solar forcing for CMIP6 (v3.2). Geoscientific Model Development, *10*(6), 2247−2302. https://doi.org/10.5194/gmd-10-2247-2017

Maxwell, R.M., Chow, F.K., & Kollet, S. J. (2007). The groundwater-land-surface-atmosphere connection: soil moisture effects on the atmospheric boundary layer in fully-coupled simulations. Advances in Water Resources, 30(12). https://doi.org/10.1016/j.advwatres.2007.05.018, 2007.

Maxwell, R. M., & Kollet, S. J. (2008). Interdependence of groundwater dynamics and land-energy feedbacks under climate change. Nature Geoscience, 1(10), 665–669. https://doi.org/10.1038/ngeo315

Maxwell, R. M., & Condon, L. E. (2016). Connection between groundwater flow and transpiration partitioning. Science, 353(6297), 377–380. https://doi.org/10.1126/science.aaf7891

Meinshausen, M., Vogel, E., Nauels, A., Lorbacher, K., Meinshausen, N., Etheridge, D. M., et al. (2017). Historical greenhouse concentrations for climate modelling (CMIP6). Geoscientific Model Development, 10, 2057–2116. https://doi.org/10.5194/gmd-10-2057-2017.

Millward-Hopkins J, Tomlin A, Ma L, Ingham D and Pourkashanian M (2011) Estimating aerodynamic parameters of urban-like surfaces with heterogeneous building heights. Bound-Layer Meteorol, 141, 443-465.

Nilsson C, Reidy CA, Dynesius M, et al. (2005), Fragmentation and flow regulation of the world's large river systems. Science, 308:405–408.

Oleson, K. (2013). Technical description of version 4.5 of the Community Land Model (CLM), Natl. Cent. for Atmos, Res., Tech. Note NCAR/TN-503+ STR.

Postel SL, Daily GC, Ehrlich PR. (1996), Human appropriation of renewable fresh water. Science, 271:785–788.

Rockström J, Steffen W, Noone K, et al. (2009), A safe operating space for humanity. Nature, 461:472–475.

Rodell, M., and Coauthors, 2004: The Global Land Data Assimilation System. Bull. Amer. Meteor. Soc., 85, 381–394, doi:https://doi.org/10.1175/BAMS-85-3-381.

Sailor DJ. A review of methods for estimating anthropogenic heat and moisture emissions in the urban environment(J). International Journal of Climatology, 2011, 31(2): 189-199.

Sailor DJ, Lu L. A top-down methodology for developing diurnal and seasonal anthropogenic heating profiles for urban areas(J). Atmospheric Environment, 2004, 38(17): 2737-2748.

Sanderson EW, Jaiteh M, Levy MA, et al. (2002), The human footprint and the last of the wild. BioScience, 52:891–904.

Stevens, B., Fiedler, S., Kinne, S., Peters, K., Rast, S., Musse, J., et al. (2017). MACv2-SP: A parameterization of anthropogenic aerosol optical properties and an associated Twomey effect for use in CMIP6. Geoscientific Model Development, *10*(1), 433–452. https://doi.org/10.5194/gmd-10-433-2017

Van Cappellen, P., & Maavara, T. (2016). Rivers in the Anthropocene: Global scale modifications of riverine nutrient fluxes by damming. Ecohydrology & Hydrobiology, 16, 106–111. https://doi.org/10.1016/j.ecohyd.2016.04.001.

Vitousek PM, Mooney HA, Lubchenco J, et al. (1997), Human domination of Earth's ecosystems. Science, 277:494–499.

Vörösmarty CJ, McIntyre PB, Gessner MO, et al. (2010), Global threats to human water security and river biodiversity. Nature, 467:555–561.

Wagener T, Sivapalan M, Troch PA, et al. (2010), The future of hydrology: an evolving science for a changing world. Water Resour Res, 46:W05301.

Willmott, C. J. and K. Matsuura (2001) Terrestrial Air Temperature and Precipitation: Monthly and Annual Time Series (1950 - 1999), http://climate.geog.udel.edu/~climate/html_pages/README.ghcn_ts2.html.

Woli, P., Hoogenboom, G., & Alva, A. (2016). Simulation of potato yield, nitrate leaching, and profit margins as influenced by irrigation and nitrogen management in different soils and production regions. Agricultural Water Management, 171, 120–130. https://doi.org/10.1016/j.agwat.2016.04.003

Xie, P. P., and P. A. Arkin, (1997), Global precipitation: A 17-year monthly analysis based on gauge observations, satellite estimates, and numerical model outputs. Bull. Amer. Meteor. Soc., 78, 2539–2558.

Xie Zhenghui, Zhenhua Di, Zhendong Luo, et al. (2012), A quasi-three-dimensional variably saturated groundwater flow model for climate modeling. J. Hydrometeor, 13, 27–46. doi: http://dx.doi.org/10.1175/JHM-D-10-05019.1

Xie Zhenghui, Shuang Liu, Yujin Zeng, et al. (2018) A high-resolution land model with groundwater lateral flow, water use and soil freeze-thaw front dynamics and its applications in an endorheic basin, 2018. Journal of Geophysical Research-Atmospheres, 123. doi: 10.1029/2018JD028369.

Yu, Y., Xie, Z. H., & Zeng, X. B. (2014). Impacts of modified Richards equation on RegCM4 regional climate modeling over East Asia. Journal of Geophysical Research: Atmospheres, 119, 12,642–12,659. https://doi.org/10.1002/2014JD021872

Zeng, Y., Zhenghui Xie, Yan Yu, et al. (2016a), Ecohydrological effects of stream–aquifer water interaction: a case study of the Heihe River basin, northwestern China, 2016a. Hydrology and Earth System Sciences, 20, 2333-2352, doi:10.5194/hess-20-2333-2016.

Zeng, Y., Xie, Z., Yu, Y., et al. (2016b), Effects of anthropogenic water regulation and groundwater lateral flow on land processes, J. Adv. Model. Earth Syst., 8, 1106–1131, doi:10.1002/2016MS000646.

Zeng, Y., Xie, Z., and Zou, J. (2017), Hydrologic and climatic responses to global anthropogenic groundwater extraction. J. Climate, 30, 71–90, doi: 10.1175/JCLI-D-16-0209.1.

Zeng, Y., Xie, Z., Liu, S., et al. (2018). Global land surface modeling including lateral groundwater flow. Journal of Advances in Modeling Earth Systems, 10, 1882–1900. https://doi.org/ 10.1029/2018MS001304.

Zou Jing, Zhenghui Xie, Yan Yu, et al. (2014), Climatic reponses to anthropogenic groundwater exploitation: a case study of the Haihe River Basin, Northern China, 2014. Climate Dynamics. 42:2125-2145

Zou Jing, Zhenghui Xie, Cheezheng Zhan, et al. (2015), Effects of anthropogenic groundwater exploitation on land surface processes: A case study of the Haihe River Basin, Northern China, 2015. Journal of Hydrology. 524: 625-641.

Zou, J., Xie, Z. H., Yu, Y., Zhan, C. S., & Sun, Q. (2014). Climatic responses to anthropogenic groundwater exploitation: a case study of the Haihe River Basin, Northern China. Climate Dynamics, 42(7-8), 2125-2145. https://doi.org/10.1007/s00382-013-1995-2

Table 1. Description of the used simulations

Simulation	**Model Used**	**Period**	**Number of ensembles**
AMIP	CAS-FGOALS-g3 Land/Atmosphere component	1979–2014	5
CTL	Same as AMIP with FTF	1976–2014	3
GC	Same as AMIP with FTF, GLF	1976–2014	3
LGC	Same as AMIP with FTF, GLF, HWR	1976–2014	3
NP	CAS-FGOALS-g3 Land/Atmosphere component with bio-geochemical and nitrogen transport module	1960–2014	1

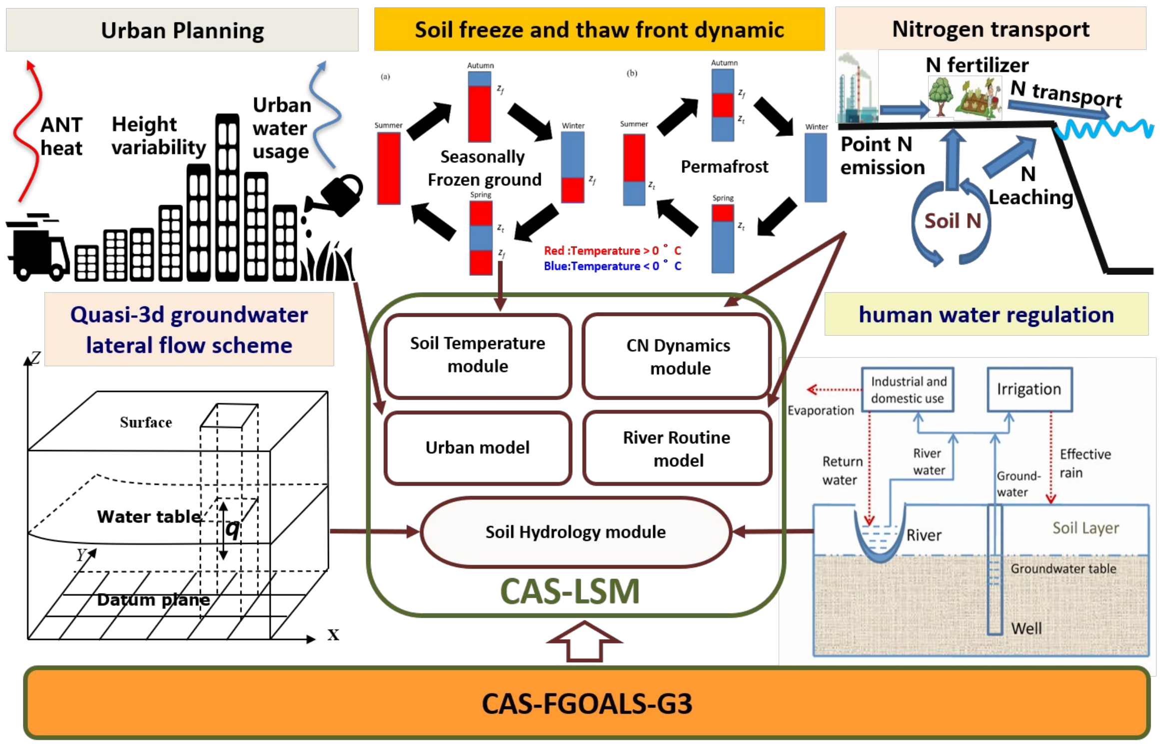

Figure 1. Schematic diagram of the land model CAS-LSM with GLF, human water use, soil FTFs, nitrogen transport, and urban planning. In the upper left panel is an illustration of the urban planning, which includes anthropogenic heat, urban water usage, and the surface roughness height scheme that considers height variability. In the upper middle panel is an illustration of the soil freeze and thaw front dynamic, while in the upper right panel, an illustration of the anthropogenic nitrogen discharge and river transport is given. In the lower left panel, an illustration of the quasi-3D GLF is presented, while the illustration in the lower right panel shows the human water use.

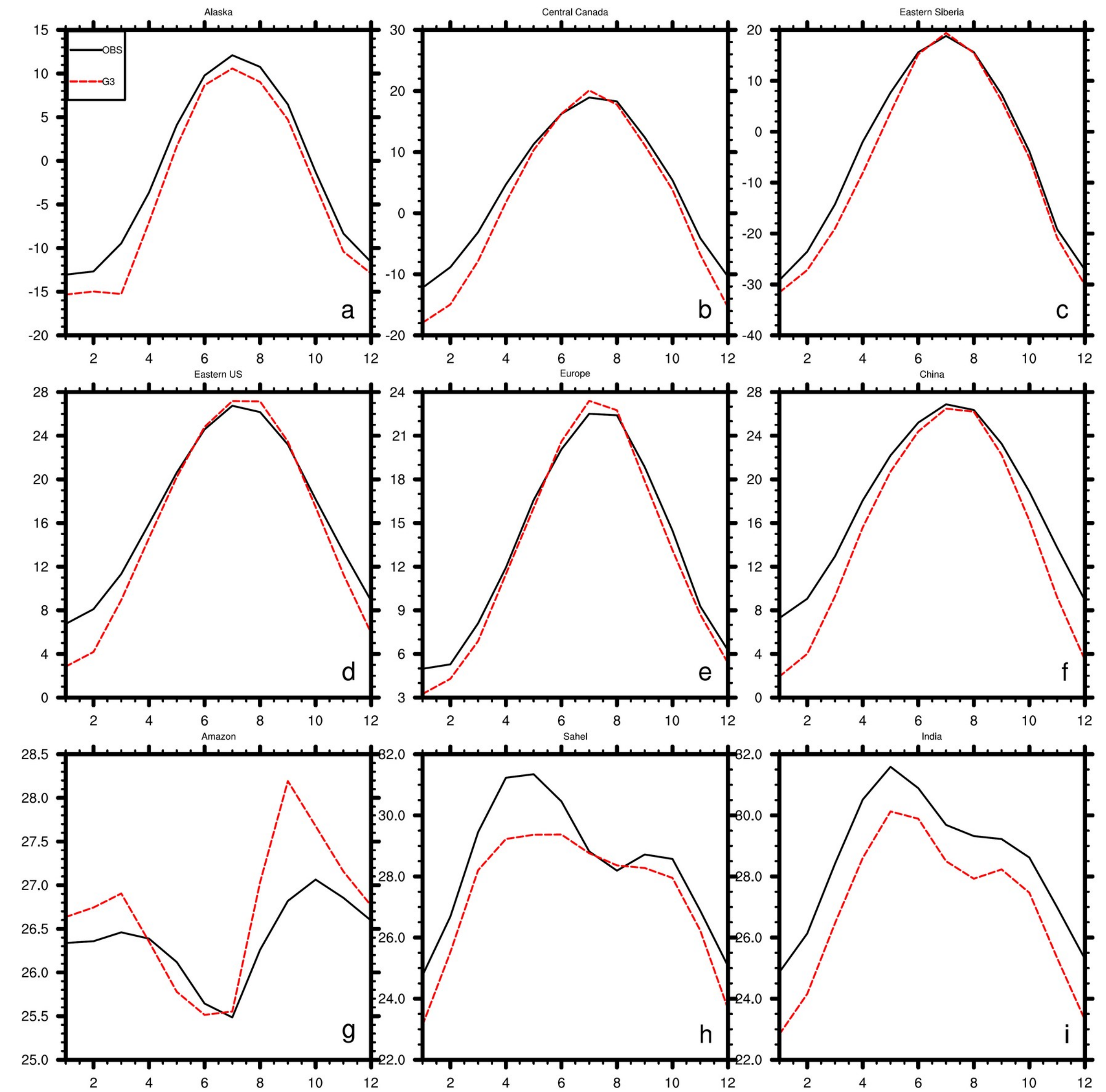

Figure 2. Climatological annual cycle of the 2-m air temperature for selected regions from CAS-FGOALS-g3 and observations from Matsuura and Willmott (2001). Regions are defined as follows: Alaska (56°–75°N, 167°–141°W), Central Canada (46°–61°N, 123°–97°W), eastern Siberia (51°–66°N, 112°–138°E), eastern United States (27°–47°N, 92°–72°W), Europe (37°–57°N, 0°–32°E), China (18°–42°N, 100°–125°E), Amazon (14°S–5°N, 74°–53°W), Sahel (4°–19°N, 0°–32°E), and India (4°–28°N, 68°–94°E).

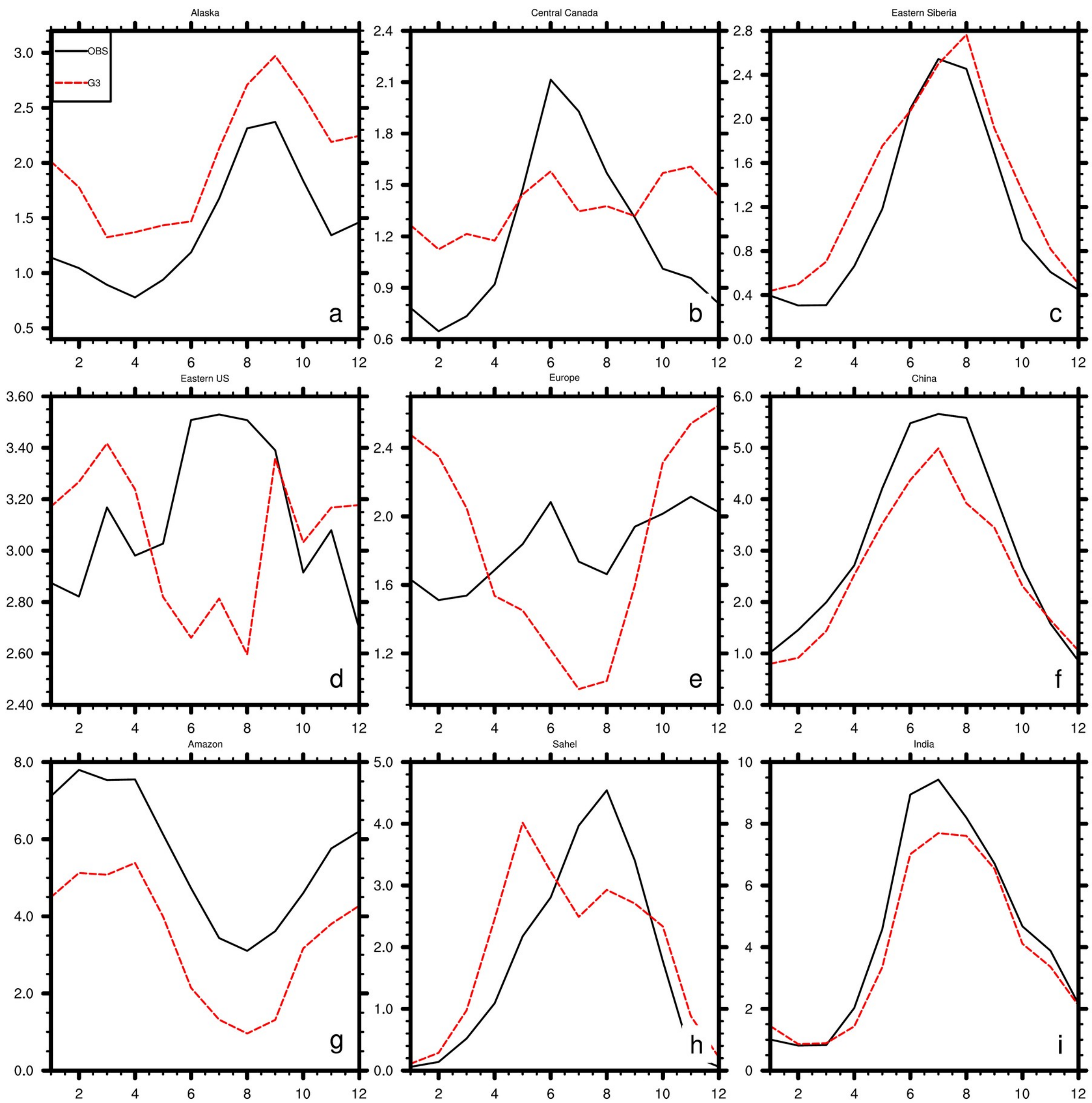

Figure 3. As in Fig. 2, but for precipitation. CMAP is the Climate Prediction Center (CPC) Merged Analysis of Precipitation 1979–2009 monthly time series at 2.5° × 2.5° (Xie and Arkin 1997).

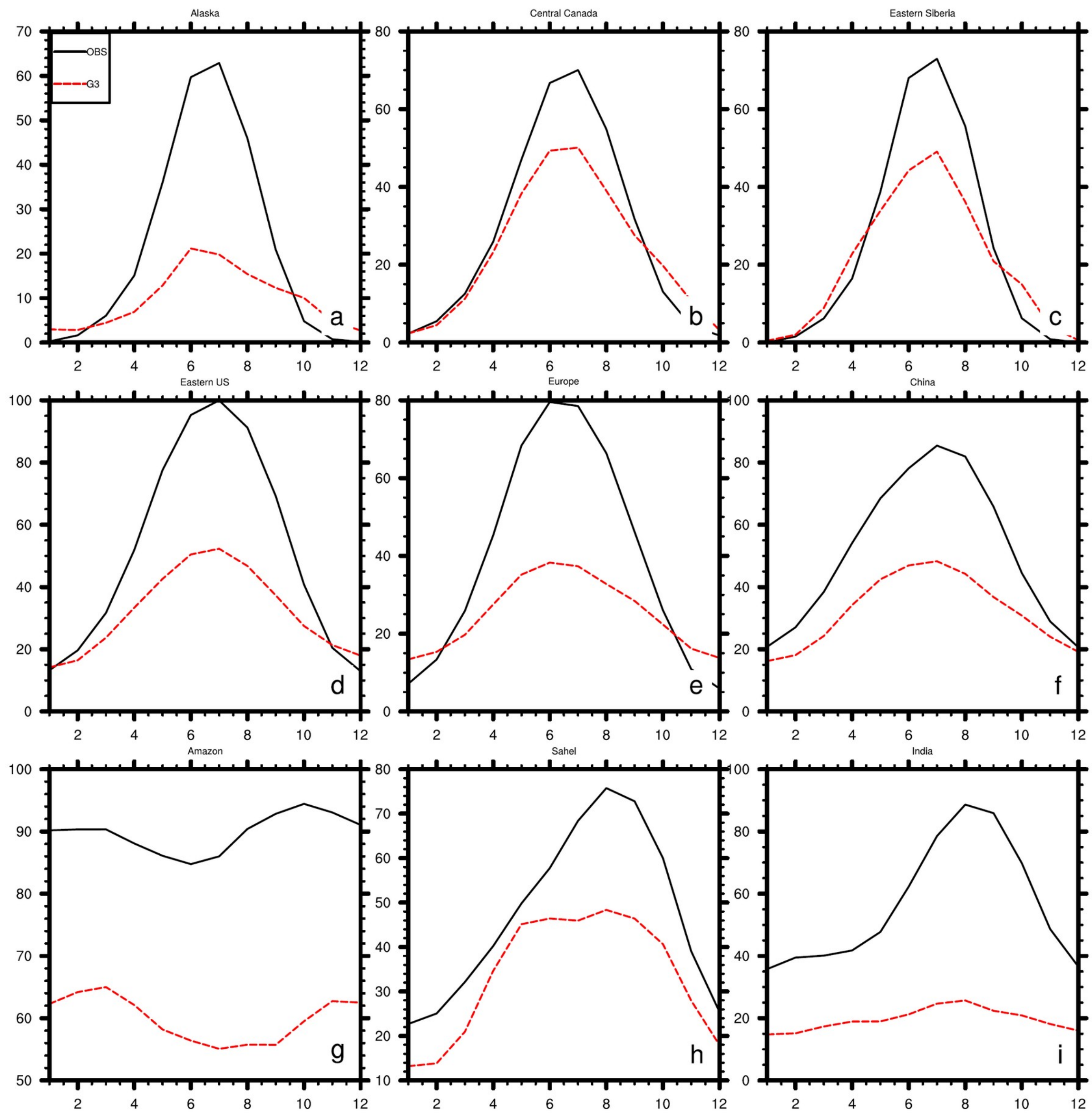

Figure 4. As in Fig. 2, but for the latent heat flux. The observational data are from FLUXNET-MTE (Jung et al., 2009, 2010). The FLUXNET-MTE data are from the FLUXNET network of eddy covariance towers, which have been upscaled to monthly evapotranspiration on a 0.5° × 0.5° grid (Jung et al. 2010) using the MTE approach described by Jung et al. (2009) (1982–2004 average).

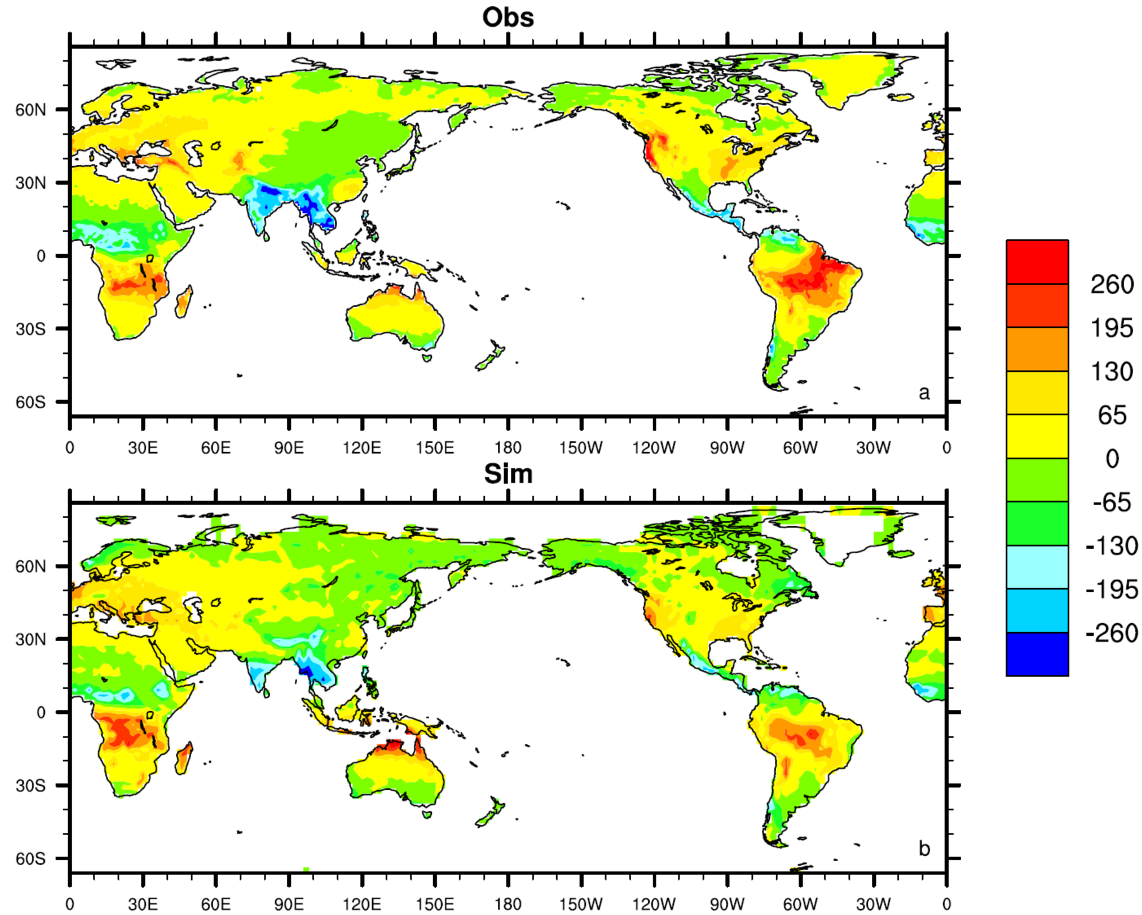

Figure 5. Difference in the mean soil water content (mm) between spring (MAM) and fall (SON) for (a) GLDAS 2 and (b) CAS-FGOALS-g3, for 1980–1999.

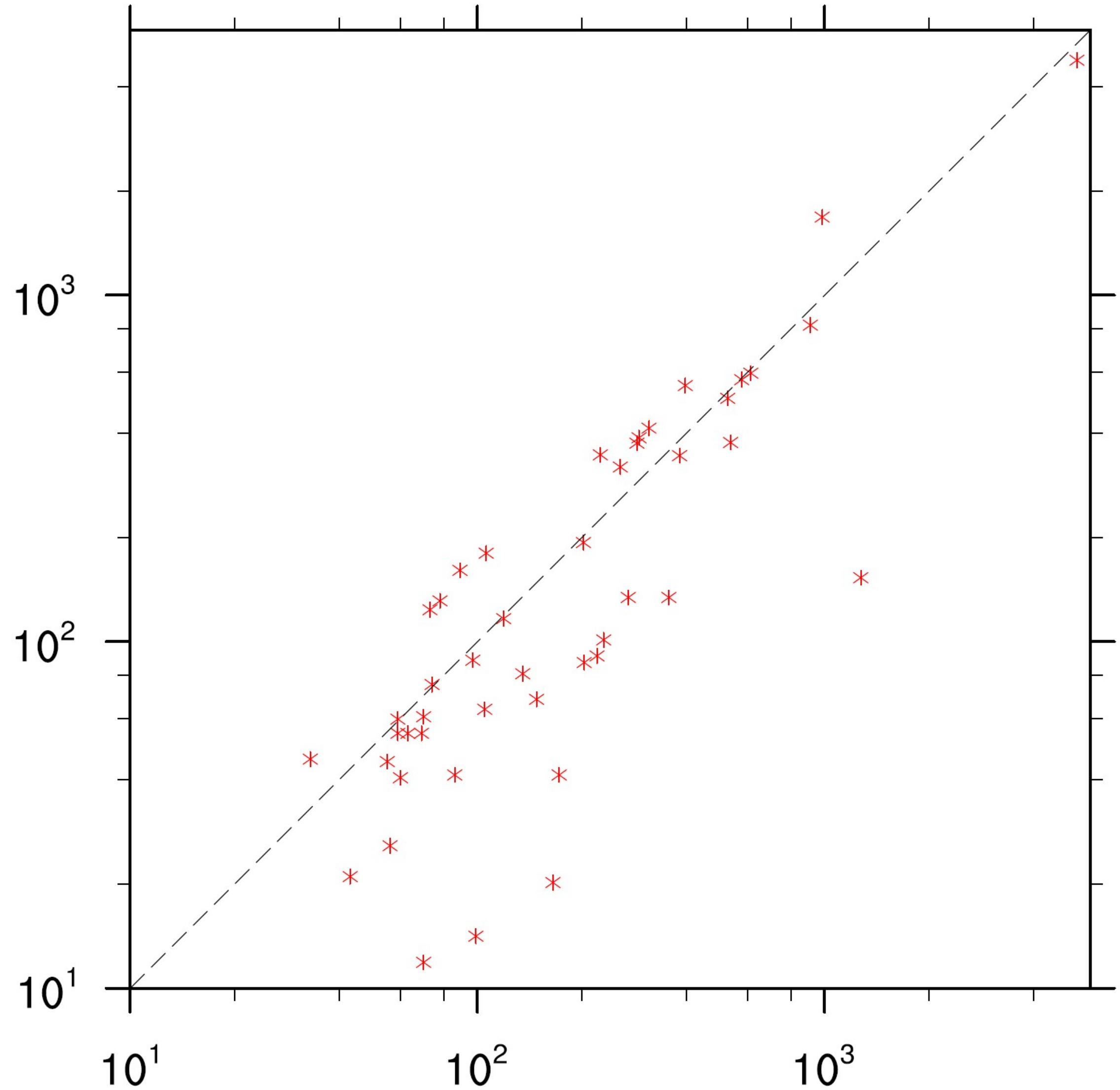

Figure 6. Comparison of the observed and modeled annual river discharge for the world's largest 50 rivers from CAS-FGOALS-g3. The Niger and Zambezi Rivers have been excluded because their observed discharges are unrealistically low (Qian et al. 2006). The observed discharge data are from Dai and Trenberth (2002).

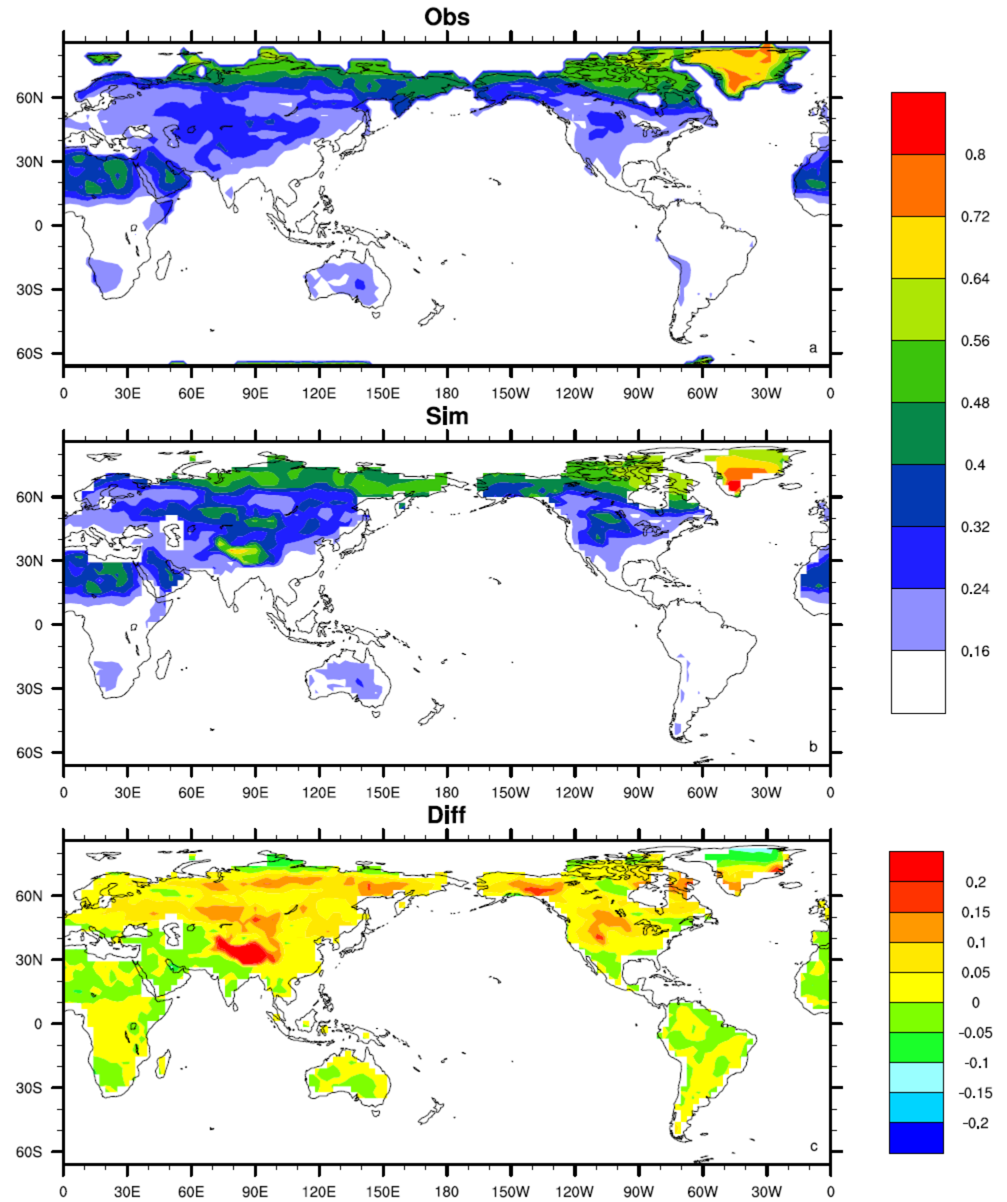

Figure 7. Maps of the annual mean all-sky albedo (calculated as the reflected solar radiation divided by the incident solar radiation) for CAS-LSM versus MODIS observation for the years 2001–2002. For each grid cell, only months where the monthly mean solar radiation (S_{atm}, 100 $W \cdot m^{-2}$) are included in the albedo calculation, which reduces, but does not eliminate, the impact of the low snow albedo bias in the MODIS data at high solar zenith angles (Wang and Zender 2010). The MODIS all-sky albedos

were derived from the black-sky (direct) and white sky (diffuse) near-infrared and visible waveband albedos by weighting them according to the CAS-LSM partitioning of S_{atm} into these components.

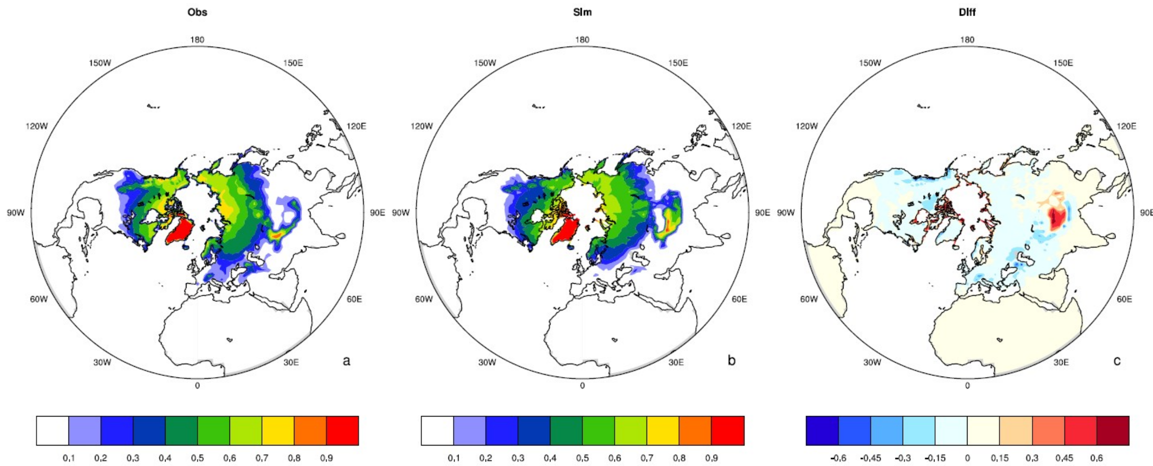

Figure 8. Comparison of the (a) observation (OBS) and (b) modeled (SIM) snow cover extent and (c) their difference (SIM-OBS) for the Northern Hemisphere. The OBS data are from the 1° × 1° Northern Hemisphere EASE-Grid Snow Cover and Sea Ice Extent data set (Brodzik and Armstrong, 2013), which were interpolated into a 2° × 2° grid for comparison.

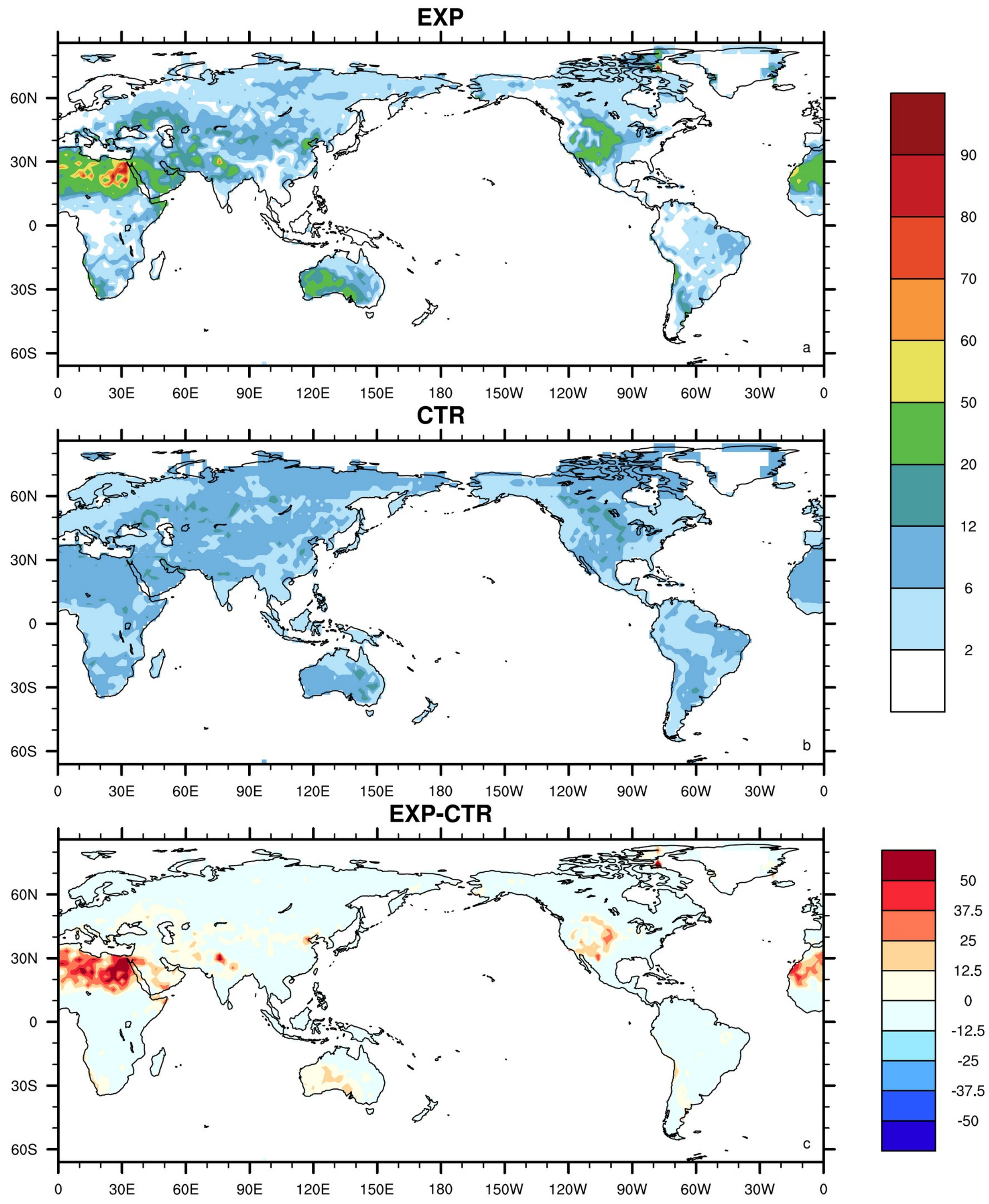

Figure 9. Global equilibrium groundwater table depth patterns from the (a) EXP simulation, (b) CTR simulation, and (c) their difference (EXP-CTR) for 1979–1999.

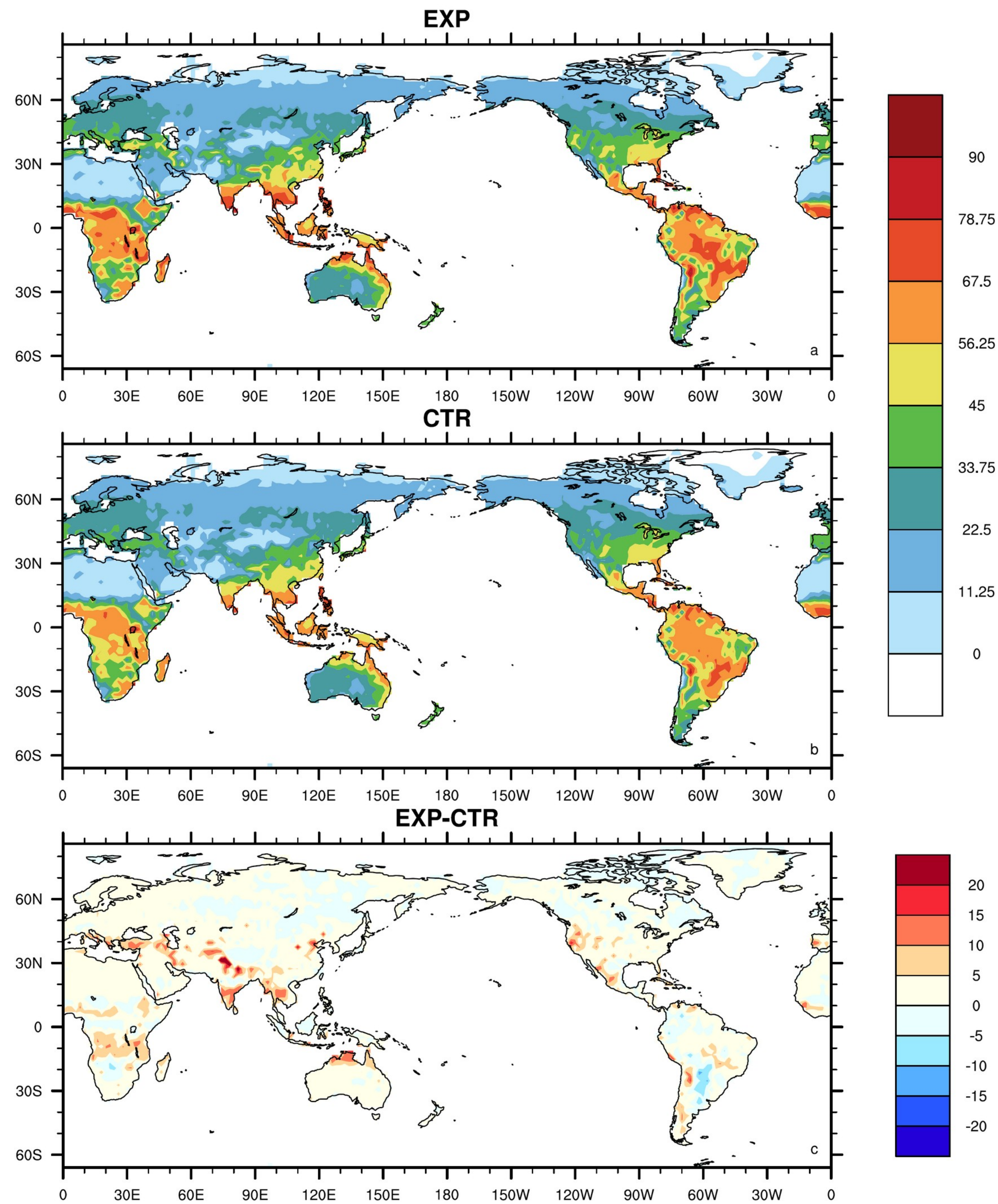

Figure 10. Latent heat flux from the EXP and CTR simulations ($W \cdot m^{-2}$).

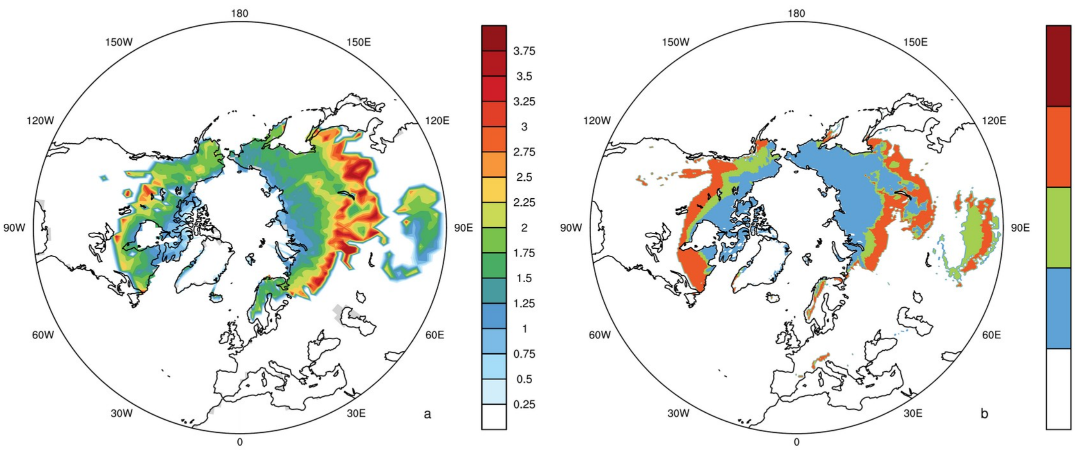

Figure 11. (a) Simulated permafrost active layer depth (defined by the maximum of the monthly thaw depth in the permafrost region, m) and (b) the observed permafrost spatial distribution from International Permafrost Association (IPA). The 0 to 4 in (b) stand for no permafrost, continuous (90–100%), discontinuous (50–90%), sporadic (10–50%), and isolation (<10%), respectively.

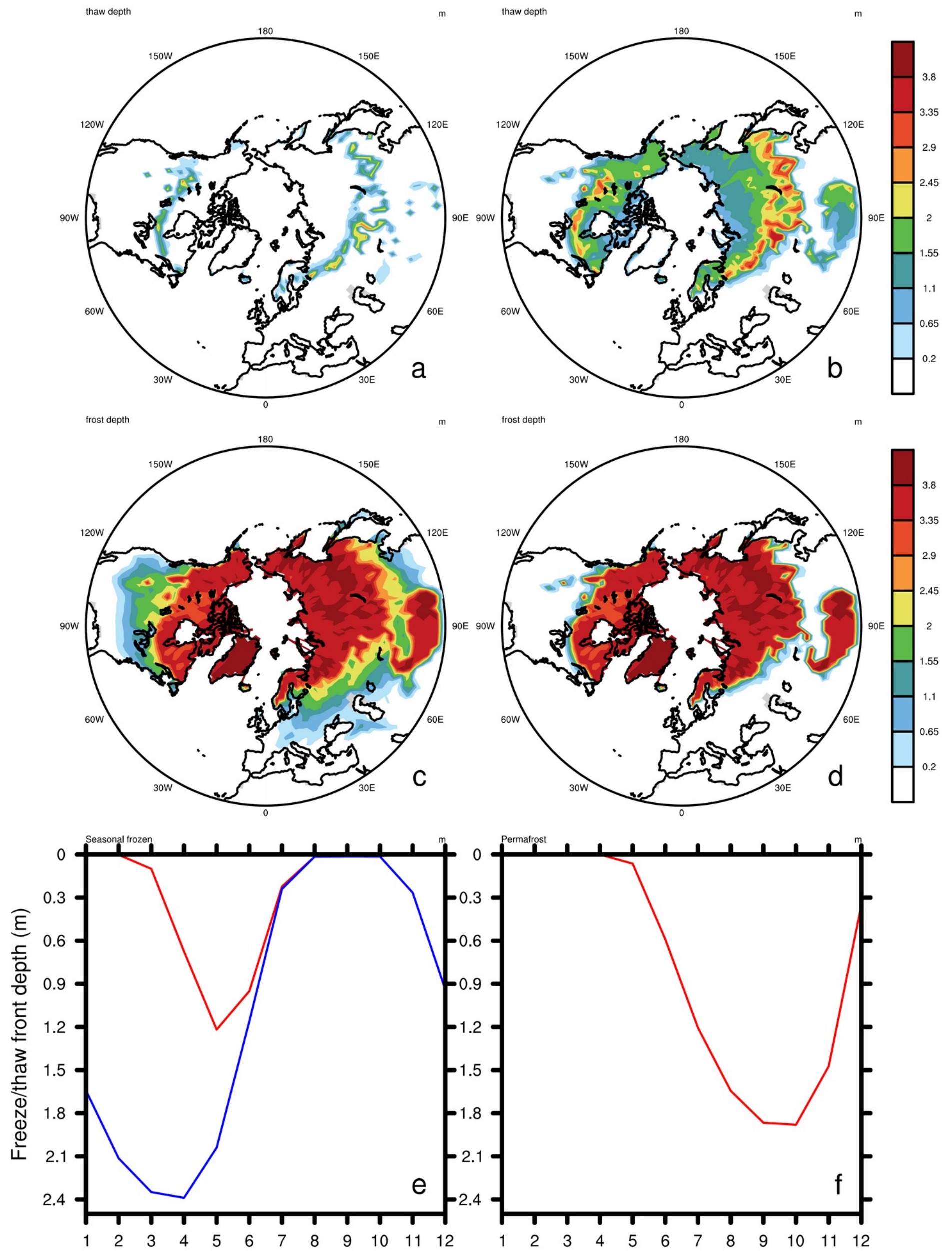

Figure 12. The February and August (a–b) thaw depth, (c–d) frost depth, and (e–f) the seasonal cycle for two regions containing seasonally frozen ground and permafrost, respectively.

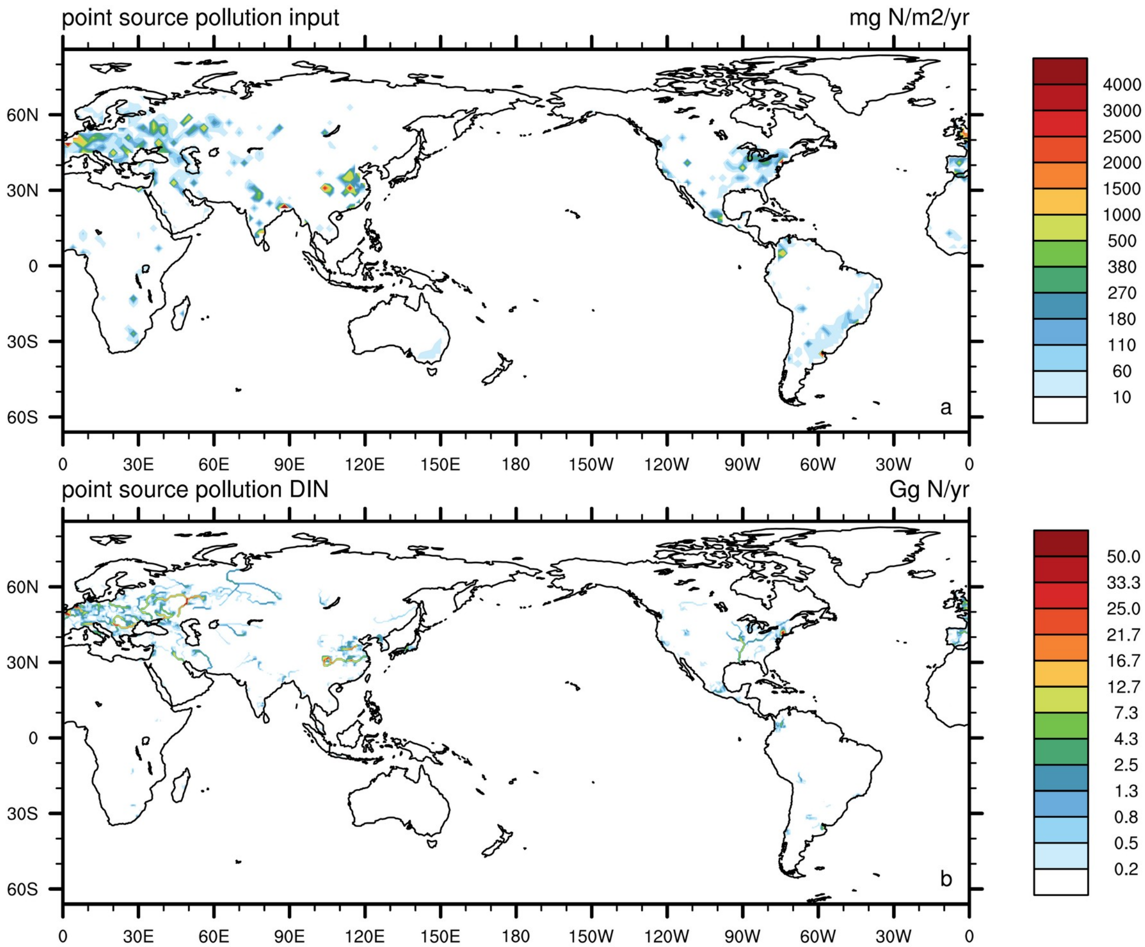

Figure 13. Global climatological distribution of the point source pollution input ($mg \cdot N \cdot m^{-2} \cdot yr^{-1}$) and its effect on riverine DIN transport ($Gg \cdot N \cdot yr^{-1}$) for 1970–2010.

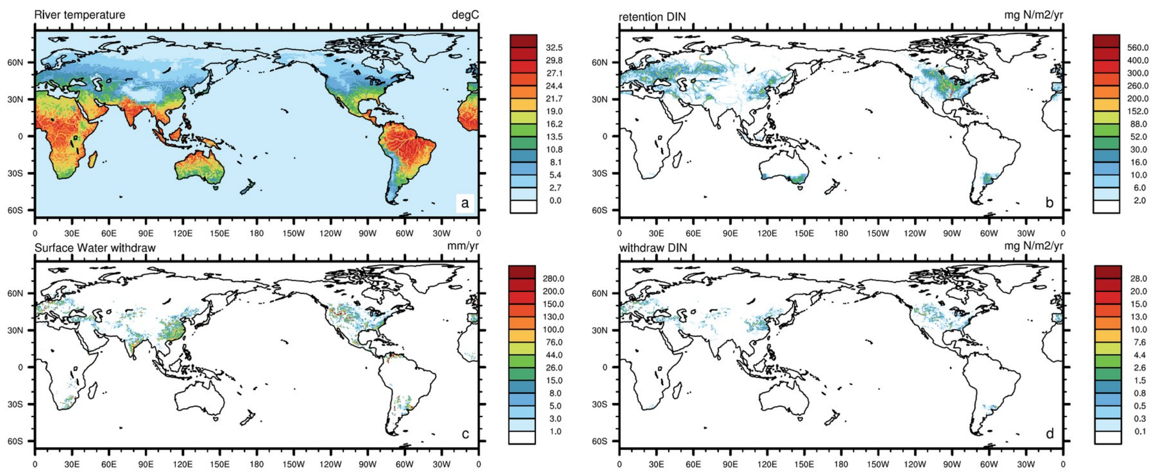

Figure 14. Global climatological distribution of the river temperature (°C), retained DIN ($mg \cdot N \cdot m^{-2} \cdot yr^{-1}$), surface water withdrawal ($mm \cdot yr^{-1}$), and withdrawn DIN ($mg \cdot N \cdot m^{-2} \cdot yr^{-1}$) for 1970–2010.